Multichannel, triaxial, neutron time-of-flight diagnostic for experiments at the *Z* facility

C. L. Ruiz,[1,*] D. L. Fehl,[1,†] G. A. Chandler,[1] G. Cooper,[2] B. Jones,[1] J. D. Styron,[2] and J. Torres[1]
[1]*Sandia National Laboratories, Albuquerque, New Mexico 87105, USA*
[2]*University of New Mexico, Albuquerque, New Mexico 87131, USA*

(Received 20 December 2018; accepted 9 December 2019; published 10 February 2020)

Neutron bang times t_{bang} and mean neutron speeds $\bar{u}$ have been measured at the *Z* facility for a series of D_2-filled targets, in magnetized liner inertial fusion experiments. Measurements were made by a novel neutron time-of-flight (nTOF) diagnostic, adapted for use at this facility, and consisted of detecting the neutron times in flight at seven independent scintillator–photomultiplier tube detectors (channels), located on three noncoplanar lines of sight, with distances to the neutron source varying between 690 and 2510 cm. The nTOF signals were analyzed by identifying fiducials on the detector traces to quantify the time in flight to each distance, using a nonrelativistic model for a uniformly thermalized, Maxwellian plasma distribution. The measured neutron arrival times were then linearly regressed on distance with the bang time and mean speed estimated from the fit parameters. A particular shot, 2584, is analyzed here to illustrate the method and the issues encountered in these measurements. On this particular shot, six usable channel traces were obtained. The standard errors of the parameter fits were as follows: $t_{\mathrm{bang}} = 3102.95 \pm 0.97$ ns (standard error) with six nTOF traces on the system clock and $\bar{u} = 2.1524 \pm 0.0032$ cm/ns (standard error), from which the mean, nonrelativistic, kinetic energy $\bar{E}$ of the neutrons was 2.4216 ± 0.0144 MeV (standard error). The estimates of $\bar{u}$ and $\bar{E}$ here agree within 1% of the published values for the $D(d,n)^3$He reaction. Hence, these measurements are consistent with the production of a thermalized, Maxwellian D-D fusion plasma in this experiment. The source duration was estimated to be 3.25 ± 0.84 ns (standard error) from six pulse-width measurements.

DOI: 10.1103/PhysRevAccelBeams.23.020401

I. INTRODUCTION

Inertial confinement fusion (ICF) experiments on various fusion targets have been conducted at the *Z* accelerator (*Z*) [1,2] (Sandia National Laboratories, New Mexico) for over 20 years. Of particular recent interest has been the magnetic liner inertial fusion (MagLIF) approach [3]. The attainment of a pulsed plasma source of thermonuclear DD neutrons (with a mean neutron energy of 2.45 MeV, ion temperature of 2–3 keV, duration of ~2 ns, and yield into 4π sr of $\sim 10^{12}$ neutrons) has been reported for D_2-filled targets [4–7].

The purpose of this article is to evaluate a novel neutron time-of-flight (nTOF) technique at *Z* for measuring (a) the bang time t_{bang} of neutron emission on a system clock and (b) the mean speed $\bar{u}$ of the emergent neutrons, which can be compared to the published value for a thermalized plasma driven by the $D(d,n)^3$He reaction. This article focuses more on the nTOF technique—as modified for use at the *Z* accelerator—than on interpreting the internal plasma dynamics of a given MagLIF target.

Historically, the TOF technique has become a mainstay for characterizing particle beams in steady-state experiments [8–10]. The reason is that a TOF experiment is conceptually simple: The speed u of a single particle may be estimated by measuring its time in flight $(t_{\mathrm{start}} - t_{\mathrm{stop}})$ over a known spatial distance L and constitutes a type of temporal spectrometer.

However, when applied to pulsed, particle sources, the TOF technique involves more issues: (a) The emitted speed distribution of particles spreads out with distance as faster particles spatially outdistance the slower ones, broadening the in-flight speed distribution; (b) the particle source distribution may vary significantly in time, entangling early and late speed distributions; (c) the impulse response of the detector both delays and distorts the output signal compared to the input; and (d) the overall geometry, shielding, and sensitivity of the detector may allow for the detection of backscattered and ancillary particles, not directly related to the experiment, to mask uncollided neutrons. Signal noise, of course, may be added to these effects.

*cruiz2@comcast.net
†Retired.

Most of these complications have been encountered when the TOF technique is applied to neutron-emitting, high-density–high-temperature plasmas in laser-driven, ICF experiments. However, under controlled conditions, such issues have been addressed, and the neutron (nTOF) technique has estimated t_{bang} (the starting time of neutron production on a system clock); neutron yield into 4π sr; effective ion plasma temperatures; and fine temporal details of a burning plasma—on a nanosecond timescale [11–18].

A modified approach to an nTOF diagnostic was needed for work in the Z environment, where spatial- temporal x-ray and bremsstrahlung and neutron fields coexist close to the dd neutron source. This is largely due to the x rays from hot electrons and from high-voltage, pulsed-power components near the target. These can saturate an nTOF detector during a shot; and the sheer mass of Z acts as a gigantic, neutron scatterer, complicating the recorded nTOF signals.

In a novel strategy to reduce these problems, Ruiz [19] proposed to measure neutrons at several locations L_k farther out from the source so that the detectors might be able to recover from the x rays that precede the arrival of target neutrons. The penalty for measurements in the far field is, of course, pulse broadening that washes out fine details of neutron production. Yet, at longer distances, one does expect better resolution for the arrival times of previously uncollided neutrons incident on detectors and, hence, improved estimates of t_{bang} than from a single distance. Moreover, multiple arrival-time measurements, linearly proportional to L_k, should lead on average to a more reliable estimate of the mean neutron speed $\bar{u}$. However, the emphasis of this approach depends on defining the neutron times of arrival in the midst of noise and backscattered neutrons and x rays.

The remainder of this article is organized as follows: (a) Section II describes the spatial deployment of neutron detectors and their characterization at the Z for MagLIF experiments, together with raw data from shot 2584 that illustrate several of the experimental issues, noted above; (b) Sec. III describes a model for neutron pulse shapes according to the theory of Brysk [11] for a uniform temperature and particle density, Maxwellian DD plasma and accounts for the IRF of the detectors, together with definitions of arrival times (expanded in the Appendix); (c) Sec. IV displays the results of linearly fitting the nTOF arrival data and estimates t_{bang} and $\bar{u}$; and (d) Sec. V discusses alternative estimates of t_{bang}, $\bar{u}$, and their uncertainties, based on simple assumptions of time and distance errors as well as an estimate of the source duration. *A priori*, we anticipate individual, distance uncertainties $\delta L \approx 1$ cm at best (Sec. II A) and uncertainties in time $\delta t \approx 1$ ns (Appendix). "Back-of-the-envelope" uncertainty estimates of pertinent parameters are listed in Table IV.

II. EXPERIMENTAL CONFIGURATION AND RAW DATA 2584

A. Geometry and detector characterization

Figure 1 shows a perspective view of the Z accelerator at the Z facility. Overall, the accelerator is cylindrically symmetric about a vertical center axis passing through a concentric, vacuum target chamber (3.66 m in diameter and 7.62 m high); a MagLIF target is placed at the center of this chamber. Marx generators, storage capacitors, pulse-forming lines, switches, and a plastic insulation stack surround the target chamber. These components are variously immersed in oil or water or evacuated. Outside the target chamber, in spherical-polar coordinates, nTOF detectors were situated at several radial line-of-sight distances L_k and different angular locations as shown in Table I. Detectors at 689.64 and 785.98 cm were located in a pit below the center of the accelerator tank, and the other detectors were above. The choice of multiple, noncoplanar line-of-sight axes allowed for angular consistency and output asymmetry checks. CH2 and Pb collimators were placed near the neutron source as well as near the detectors, except for the farthest detector at 2510 cm from the source, which lacked heavy shielding. Table I lists the channel names for the detectors, their angular locations, and distances L_k around the target.

Radial source-to-scintillator distances L_k were measured with a graduated, steel tape which was (just) able to resolve length increments of ~0.07 cm (1/32 inches), with an ascribed accuracy to L_k of not better than ± 1 cm. Such uncertainties δL translate into ~0.5 ns arrival-time uncertainties for 2.45 MeV neutrons. (Despite such estimates δL, Table I retains distance values to 0.01 cm to reduce round-off errors in the statistical analyses below.)

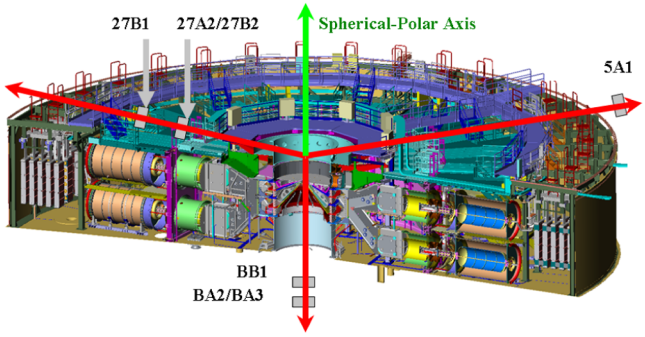

FIG. 1. Perspective view of the Z accelerator for MagLIF target experiments and of the lines of sight used for nTOF measurements (not to scale). Depicted inwards from the outer oil-tank wall are Marx generators, storage capacitors, pulse-forming lines, and the insulator stack; not shown is the MagLIF target-chamber insert itself. Labeled NTOF detector locations are shown on the various diverging lines of sight and correspond to Table I. The origin of the spherical-polar coordinate system coincides with the target, and its polar axis (green) is coincident with the cylindrical symmetry axis of the target chamber.

TABLE I. Source-to-detector distances L_k (cm) and angular locations of nTOF detectors for MagLIF shot 2584 in standard spherical-polar coordinates. Azimuthal angles were measured relative to a fixed, locally defined direction.

Distance (cm) L,k	Channel name	Azimuth (deg)	Polar (deg)
689.64	BB1	···	180
785.98	BA2	···	180
785.98	BA3	···	180
944.56	27B2	270	78
1145.85	27B1	270	78
2510.00	5A1	50	78

Altogether, seven identically designed detectors were used for nTOF studies. Each consisted of a 7.62-cm-diameter, 2.54-cm-thick (1% quenched) BC-422Q scintillator, coupled via a 25.4-cm-long, ultra-violet-transmission Lucite light guide to the photocathode of Hamamatsu R5946-MOD4 mesh-type photomultiplier tube (PMT). Traces were recorded by 8-bit, 1 GHz digitizers with 0.25 ns dwell times. The impulse response function of these detectors has been studied with cosmic rays by Bonura and Ruiz [20] and is generically depicted in Fig. 2 with labeled points of interest: an initial start-time "toe," a "foot" (or dead time) region during which scintillator light travels to the PMT. Throughput times (toe-to-PMT signal peak) for all these detectors were calibrated [20]; they varied from ~11 to 13 ns (±0.3 ns, 1σ uncertainty) and depended on the PMT bias. By contrast, the PMT FWHM was ~3.5 ns (±0.3 ns) and only weakly dependent on the PMT bias. To properly align each trace with the zero time of the system clock, the entire throughput time of each plus cable delays were needed to be subtracted from the time base of the traces. All the detectors had unique cable and throughput delays (due to different biases) of at least 10–12 ns. Some nTOF detectors were "dual" in that two PMTs viewed the same scintillator in opposite directions; these included channels BA2/BA3 and 27A2/27B2 in Table I, of which 27A2 was lost.

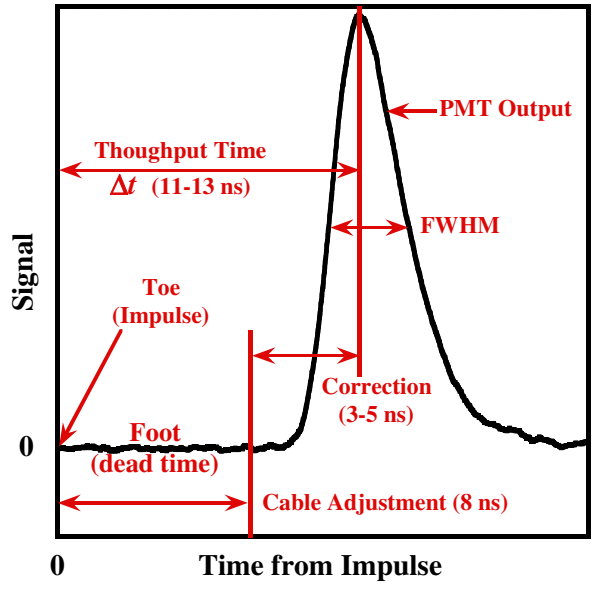

FIG. 2. A generic IRF for nTOF detectors with various features noted: an initialization time (toe), a dead time (foot) for internal light transit, and a peak of the PMT output. The throughput time Δt is defined as the time between initialization and the peak of the PMT output. For the detectors used for shot 2584, the dead time was at least 8 ns.

B. Representative raw nTOF signals

Sandia's multichannel nTOF diagnostic "piggybacked" on five, MagLIF developmental shots of varying design. All the recorded traces were shifted 8 ns earlier by cable adjustments and were labeled "raw" data. (Data labeled "corrected" data noted in Sec. IV B were further adjusted in time base by the tabulated small corrections described above.)

Figures 3–6 show time-series recorded signals $D_k(t)$ from shot 2584 and illustrate some of the experimental issues and properties encountered in fielding this diagnostic. (Four additional shots in this series yielded similar characteristics and results.) Shot 2584 obtained usable signals in six channels (Table I) of the seven fielded nTOF detectors, a not uncommon occurrence in this series and a justification for dual detectors. (The missing signal 27A2 in Fig. 1 went off the scale due to a faulty scope sensitivity setting).

Figure 3 shows the BB1 signal from the detector closest to the source (~690 cm). It illustrates why the time-resolving neutron detectors used here cannot be deployed appreciably closer to the MagLIF target: The off-scale pulse at 3000 ns corresponds to bremsstrahlung

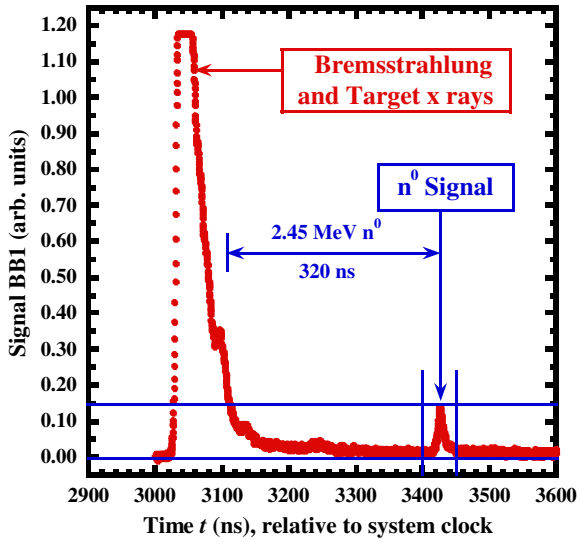

FIG. 3. Raw data from shot 2584 for channel BB1 with an early, off-scale bremsstrahlung signal and extended tail, together with a small nTOF signal.

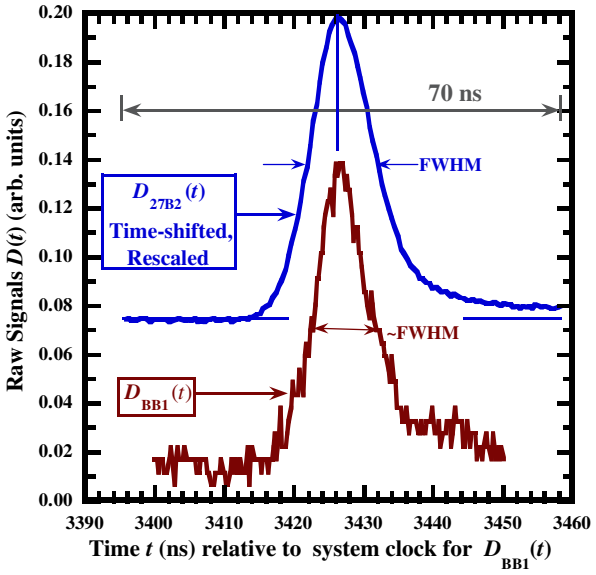

FIG. 4. Overlay comparison of noise in raw data between two nTOF channels, BB1 and 27B2. (Data from channel 27B2 have been shifted earlier by 118 ns and rescaled in this comparison).

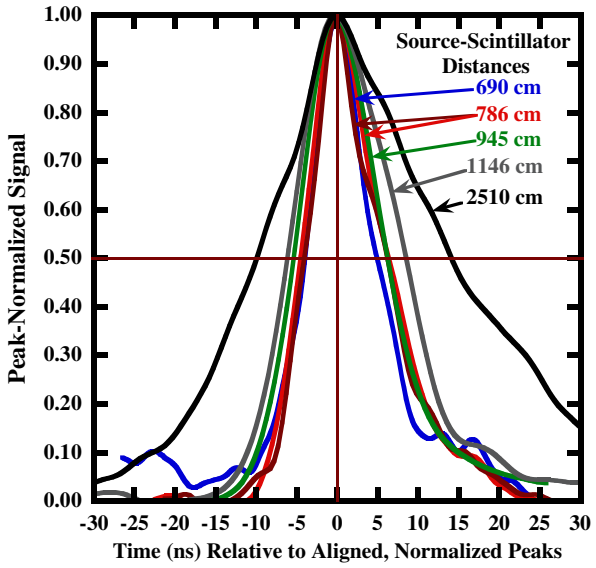

FIG. 6. Comparison of all six usable nTOF channels in shot 2584, smoothed, normalized, and aligned at the peak (t_{smoo}). The FWHM is depicted. Signals above the FWHM are roughly symmetric, with the exception of signal 5A1 at 2510 cm from the source.

from various pulsed-power components of the accelerator and possibly the MagLIF target, while the neutron pulse is the tiny peak at ~3430 ns. The figure also indicates the time in flight of a 2.45 MeV D-D neutron to the BB1 detector.

Figure 4 qualitatively compares variations in the raw signal noise in the neutron traces. Shown here are again BB1 (lower trace) and channel 27B2 (upper trace, shifted and scaled), which is located ~2 m more distant from the MagLIF target than the BB1 detector and which peaks in signal ~100 ns later than BB1. The dominant noise in BB1 is due to signal quantization in the digitizer, which was trying to capture the tiny nTOF pulse near an off-scale x-ray pulse; the noise clearly degrades the otherwise analyzable BB1 neutron signal.

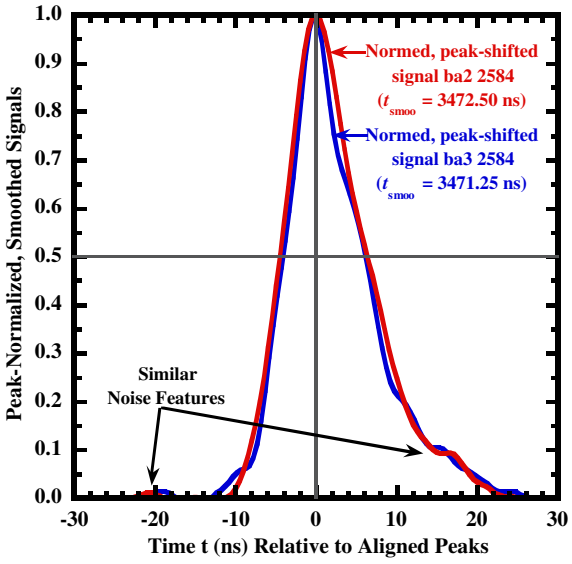

FIG. 5. Overlay comparison of (smoothed) signals from the dual, two-channel detector (BA2 and BA3). In this case, the recorded signals were closely similar in shape and separated by 1.3 ns.

Figure 5 illustrates the advantages of a dual detector as a check on signal reproducibility and a backup channel. Dual channels BA2 and BA3 at the same distance from the source are compared. The traces shown have been smoothed [21,22], aligned in time at the peak (shift ~1.3 ns), and scaled.

Figure 6 is a composite of the raw data traces obtained from all six nTOF channels in shot 2584. (These have been smoothed and aligned at the peak; cf. the Appendix.) The signals in Fig. 6 are all monomodal pulses, skewed positive (i.e., a higher falling than rising tail), increase in width (FWHM) with distance from the MagLIF target due to pulse spreading, and have most similar shapes at times within their respective FWHM. The exception is channel 5A1 at 2510 cm, which was largely unshielded and may show backscattering issues.

III. METHODS OF DATA ANALYSIS

The purpose of the analysis below is to make a case for associating a fiducial (generically, $\bar{t}_k$) with a detected neutron pulse at each distance L_k from the source. Such fiducials may then establish mean neutron arrival times at the detectors, and from them one may estimate a start time t_{bang} and mean speed $\bar{u}$—without dealing in detail with the shape of the neutron pulse. This task requires a plasma

model for neutron emission and propagation. For convenience, we assume here that for time τ the MagLIF D_2 plasma is thermalized with a constant and spatially uniform temperature T producing an internal Maxwellian distribution of neutrons and ions. The following sections seek to establish a connection between the properties of this plasma model with experimental fiducials in the nTOF traces $D_k(t)$, if noise and competing interferences can be identified and controlled.

A. A model for uncollided neutron flux in nTOF experiments

The first order of business in analyzing $D_k(t)$ in MagLIF shot 2584 is to see if the duration of the source significantly affects the arrival of neutrons at the nTOF detectors. According to Refs. [4,5], an estimate of τ in a similar shot is ~2 ns. In quadrature with nTOF arrival times (>300 ns, Fig. 3), τ contributes negligibly, and the source can be treated as instantaneous for t_{bang} and $\bar{u}$ measurements. Yet, for pulse-width measurements (9–24 ns, Fig. 6), τ may to be noticeable. (See Sec. V.)

The next step is to derive how a neutron pulse in this analysis spreads out in an nTOF experiment—i.e., an impulse response $G_k(t)$ for neutrons arriving at location L_k and at time $\hat{t}_k$ (relative to t_{bang}). This is based on Brysk's theoretical study [11] of nonrelativistic, uniform temperature and particle density, Maxwellian plasmas, which found that, for deuterium plasmas interacting by the $D(d,n)^3$He-reaction, the differential neutron energy spectrum $\partial N/\partial E$ of neutrons emerging from the plasma is isotropic and of the form

$$\frac{\partial N}{\partial E} \approx A \exp\left[-\frac{(E-\bar{E})^2}{\sigma_T^2}\right], \tag{1}$$

where $\bar{E}$, σ_T, and E have units of energy; the constant $A > 0$ has units of neutron density per unit energy; and σ_T represents the energy spread for temperature T. Equation (1) is a Gaussian distribution in neutron kinetic energy E, and $\bar{E}$ is the mean neutron kinetic energy as well as the statistical mode. Emergent neutrons that do not interact with each other or surrounding materials on the way to the nTOF detector preserve this information about the internal plasma conditions ($\bar{E}$ and T), and we refer to them collectively as uncollided neutrons. (Relativistic computations of $\partial N/\partial E$ have been made by Munro [12] and Ballabio [13], who found asymmetries at much higher neutron energies. But, such a calculation is unneeded for the DD fusion neutrons here, because $\bar{E} = 2.45$ MeV is much smaller than $m_0c^2 = 939$ MeV.)

Using the chain rule of calculus and $\partial N/\partial E$, one can derive the temporal shape $G_k(t)$ of uncollided incident neutrons at location L_k for this model:

$$G_k(t) \cong -A \cdot B\left(\frac{2\bar{E}}{\hat{t}_k}\right)\left(\frac{\hat{t}_k}{t}\right)^3 \exp\left[-\frac{\bar{u}^2\bar{E}^2}{\sigma_T^2 L_k^2}(t-\hat{t}_k)^2\right]. \tag{2}$$

Here, t is the observation time (referenced to t_{bang}) and corresponding to kinetic energy E in Eq. (1); the parameters $\bar{E} = 2.45$ MeV, $\bar{u} \equiv \sqrt{2\bar{E}/m_0} \approx 2.2$ cm/ns, $m_0 = 939$ MeV/c^2, and $\hat{t}_k \equiv L_k/\bar{u}$ are the theoretical mean neutron kinetic energy, its corresponding mean speed, its rest mass, and its mean flight time, respectively.

Several aspects of Eq. (2) need emphasis: (a) $G_k(t)$ is proportional to the input of uncollided neutrons at the upstream face of the kth nTOF detector (the constant $B > 0$ represents geometric factors); (b) in form, $G_k(t)$ is very nearly Gaussian, provided that neutrons from the source are emitted nearly instantaneously and if the observation time t is close to $\hat{t}_k$ (e.g., from Fig. 4, the half width of the BB1 neutron signal is ~5 ns and its flight time is ~320 ns, giving an observation ratio $|t-\hat{t}_{\text{BB1}}|/\hat{t}_{\text{BB1}} \approx 1.5\%$); and, most importantly, (c) the theoretical mean time $(\bar{u})^{-1}L_k$ and width $(\sigma_T/\bar{u}\,\bar{E})L_k$ of $G_k(t)$ increase linearly with L_k, which obtains experimentally. The parameters σ_T, $\bar{u}$, and $\bar{E}$ all connect back to the source plasma.

B. Detector effects in the measurements $D_k(t)$

Experimentally, one does not measure the uncollided-neutron signal $G_k(t)$ in Eq. (2), because the measured signals $D_k(t)$ have been distorted by the impulse response function (IRF) of the individual detectors; the detectors are also sensitive to extraneous x-ray interactions as well as to neutrons; and signal noise is present. The effects can be combined with $G_k(t)$ in this model as a convolution [21,23] equation for $D_k(t)$ as

$$D_k(t) = \underbrace{\int_{-\infty}^{\infty} R_k(t')G_k(t-t')dt'}_{R_k * G_k} + s_k(t) + \varepsilon_k(t). \tag{3}$$

Here, $R_k(t)$ (presumed known) is the impulse response function of the kth detector (Sec. II A, Fig. 2); and $s_k(t)$ and $\varepsilon_k(t)$, respectively, represent interference signals (e.g., downscattered neutrons and x rays) and random signal noise. It is assumed here that (a) $R_k(t)$ and $G_k(t)$ are integrable, zero valued for $t < 0$ but positive valued for $t \geq 0$, and, hence, $R_k * G_k(t < 0) = 0$; (b) the nTOF detectors are operating linearly and independently; and (c) all signals detected in each channel superpose.

The $s_k(t)$ and $\varepsilon_k(t)$ interference terms in Eq. (3) are largely listed for completeness but not detailed here. They are site specific, requiring local mitigation, once identified. For example, at Z the x-ray contributions to $s_k(t)$ were reduced by moving the nTOF detectors farther from the neutron source; and contributions of downscattered neutrons could be reduced by shielding, collimation, and limiting the temporal range of the data analysis to the

FWHM of the output data $D_k(t)$ [17]. In principle, it may be possible to simulate the scattered neutron flux outside the Z machine with the Monte Carlo technique [14,15], but this is a particularly onerous task at Z due to the proximity and inhomogeneity of the massive accelerator to the neutron and x-ray scattering. The noise term $\varepsilon_k(t)$ in Eq. (3) is similarly site and location specific. As noted in Sec. II B, the most prevalent noise in the nTOF signals was quantization noise (BB1); it was controlled largely by averaging and smoothing techniques [21,22]. (See the Appendix below.) Glebov [14], Hatarik [15], and Murphy [16–18] have delineated similar issues for experiments at NOVA and NIF, as well as some mitigating schemes.

C. Extracting information about $G_k(t)$ from $D_k(t)$

Equation (3) models the flow of timewise information $G_k(t)$ about MagLIF-produced neutrons into the data $D_k(t)$. It is a Fredholm integral equation of the second kind and presents a redoubtable unfold problem for extracting $G_k(t)$ pointwise from $D_k(t)$. [Solutions are not unique, if they exist at all, and are complicated by the presence of noise $\varepsilon_k(t)$ and the need for appropriate, physical constraints—issues widely discussed in the literature [24–27].] In assessing nTOF data at NIF, Hatarik *et al.* [14–18] have prescribed a more analytical model of $G_k(t)$ with undetermined coefficients, based on the Brysk theory, which can be folded forward in $R_k * G_k$ to yield a fitting function for $D_k(t)$ and from which details of the plasma may be inferred.

The simpler goals of estimating $t_{\rm bang}$ and $\bar{u}$ for the MagLIF shots do not require an approximate reconstruction of $G_k(t)$. Heuristically, one wishes to identify generic, fiducial points $\bar{t}_k$ in $D_k(t)$ that are independent of the changing spread in nTOF pulses and that can be interpreted as the times of arrival of a pulse at L_k on the system clock. This condition obtains for nTOF pulses as long as $\partial N/\partial E$ remains fixed in time. Such fiducial times $\bar{t}_k$ in the data are analogous and estimate times $\hat{t}_k$ in $G_k(t)$ [Eq. (2)].

Natural candidates for $\bar{t}_k$ are times at or near the peak of the data signal. Three definitions were defined and labeled at each location L_k as follows: $\langle t\rangle_k$, the mean time value of $D_k(t)$ over its FWHM time domain; $t^k_{\rm smoo}$ at the maximum value of a smoothing function to $D_k(t)$; and $t^k_{\rm mode}$, a few-point estimate of the statistical mode of $D_k(t)$. The Appendix defines these measures and shows in a test case with channel BB1 (the noisiest signal) that all three measures showed ∼1−ns agreement (cf. Sec. IV A, Table II). We infer from the Appendix that $\delta t \approx 1$ ns for the uncertainty in measuring arrival times for these fiducial methods (cf. Sec. V.)

The definition $\langle t\rangle_k$ is particularly useful, because mathematically the mean time of $\langle R_k * G_k\rangle$ in Eq. (3) is the sum of means, $\langle R_k\rangle + \langle G_k\rangle$ [28]; so, in principle, an estimate of $\hat{t}_k$ for the arrival of $G_k(t)$ at L_k can be obtained from the knowledge of $\langle R_k * G_k\rangle$ and $\langle R_k(t)\rangle$. (The consistency of $t^k_{\rm smoo}$ and $t^k_{\rm mode}$ with $\langle t\rangle_k$ in the Appendix suggests a similar property for $t^k_{\rm smoo}$ and $t^k_{\rm mode}$, which is not mathematically justified here).

TABLE II. Raw-data arrival times at each nTOF detector distance L_k in shot 2584 by the independent fiducial methods from the Appendix. The means $\langle t\rangle_{\rm FWHM}$ were calculated from the FWHM time regions of the recorded raw traces.

Distance (cm)	t-smoo (ns)	$\langle t\rangle_{\rm FWHM}$ (ns)	t-mode (ns)
689.64	3426.50	3426.70	3426.56
785.98	3471.25	3472.10	3471.00
785.98	3472.50	3473.29	3472.50
944.56	3544.20	3544.63	3544.01
1145.85	3638.11	3638.98	3638.11
2510.00	4268.41	4270.40	4268.16

By whichever fiducial-time measure $\bar{t}_k$ that one chooses above, Eq. (3) can be transformed to the following timing equation for the nTOF signals on the system clock:

$$\underbrace{\bar{t}_k}_{\text{clock time}} - \underbrace{(\Delta t_k)}_{\text{detector}} = \underbrace{t_{\rm bang}}_{\text{clock time}} + \underbrace{(\bar{u})^{-1}L_k}_{\text{TOF}}. \tag{4}$$

Here, the fiducial time $\bar{t}_k$ of $D_k(t)$ on the system clock minus the throughput time of the detector represents $t_{\rm bang}$ on the system clock plus the time in flight of uncollided nTOF neutrons moving at the mean speed $\bar{u}$ from the source. The noise and interference signals have been suppressed.

Equation (4) can then be used as a fitting function for MagLIF shots on Z, once the fiducial times $\bar{t}_k$, distances L_k, and throughput times Δt_k for each channel have been determined. From this linear fit, one interprets the intercept as an estimate of $t_{\rm bang}$ and the slope as $(\bar{u})^{-1}$, the inverse of the mean neutron speed. It is worth emphasizing (a) that Δt_k is the entire throughput time of the kth nTOF detector and (b) that, for shot 2584, 8 ns of each detector's dead time has already been removed in the raw trace. The corresponding raw fiducial arrival times can be corrected for the individual remainders of Δt_k (∼3–5 ns), due to PMT bias settings and manufacturing differences, and also fit to Eq. (4).

IV. RESULTS

A. Comparison of raw neutron arrival times for all channels and fiducial methods

Table II compares the raw-data arrival times for each of the six usable nTOF detectors in shot 2584 by distance and fiducial method. The table reflects similar agreements in time ($\delta t \lesssim 1$ ns) among various methods as seen in the Appendix. An exception to this trend is the point $\langle t\rangle_{5A1}$ at 2510 cm, differing from $t^{5A1}_{\rm mode}$ and $t^{5A1}_{\rm smoo}$ by ∼2 ns; as noted, this detector was sparsely shielded, and its trace may be

showing interference from scattered neutrons and x rays. [In the following, neither removing nor weighting this datum in Eq. (4) improved the fit, so the point was retained in the final analysis, an unresolved issue. The effect of this discrepancy on the t_{bang} estimate is ~0.33 ns; cf. Sec. V].

B. Estimating t_{bang} for neutrons

Postshot estimates of t_{bang} began by fitting raw arrival-time data in Table II upon distances L_k because (a) the remaining IRF corrections were both similar to each other and small (~3–5 ns) compared to the DD neutron flight times (>350 ns); and (b) we wished to see what effect such corrections made on the fit parameters t_{bang} and $\bar{u}$ in Eq. (4) when the corrections were finally made. Equal weighting was used for these fits, and the fit residuals statistically characterized and checked by a goodness-of-fit test criterion.

Figure 7 shows the regression of $\langle t\rangle^k_{FWHM}$ upon L_k, where the distances were taken as exact. (This procedure falls within the Berkson regression model, even though both axes have uncertainties [29–31].) In this figure, dotted circles denote raw arrival times, the blue line represents the fit, and the red lines indicate statistical 95% confidence intervals for single points on the fit, magnified by a factor of 20 for visibility [29,32]. (Corresponding plots for the other arrival-time estimates, t^k_{Mode} and t^k_{smoo} vs L_k, are indistinguishable on this scale and not shown).

Statistical tests suggest that the regression in Fig. 7 is reasonable. First, a normal probability plot of the six

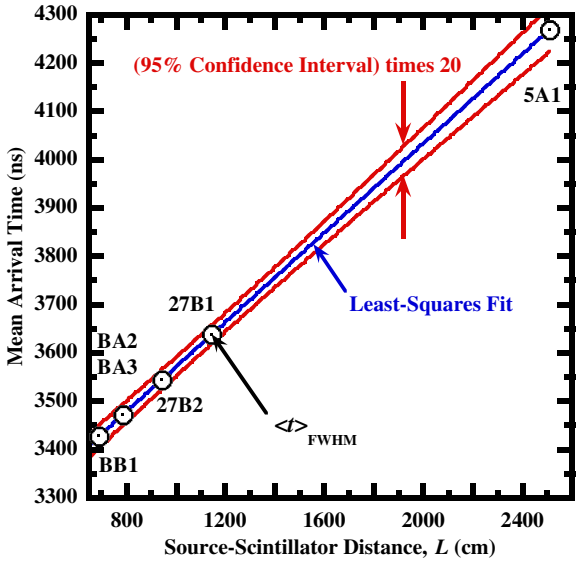

FIG. 7. Least-squares fit to the raw, mean arrival data $\langle t\rangle_{FWHM}$ for the six nTOF detectors in shot 2584. Shown (red lines) are the corresponding 95% confidence intervals (CI) for the fit at an arbitrary distance. The CI numbers have been magnified by a factor of 20 to be visible on this scale. Data channels (Table I) are noted. The fits to raw t_{Mode} and t_{smoo} arrival times are identical on this scale.

residuals (i.e., $\langle t\rangle^k_{FWHM}$ minus the fit at L_k) are consistent with a normal distribution of 0.0 ns mean and standard deviation ~1.14 ns. [For comparison, a simple quadrature sum of estimated uncertainties in time and distance, $\sqrt{(\delta t)^2 + (\bar{u})^{-2}(\delta L)^2}$, yields ~1.10 ns, where the uncertainty δt in reading $\langle t\rangle^k_{FWHM}$ taken is ~1 ns, $\delta L_k \sim 1$ ns, and $(\bar{u})^{-1} = 0.4629$ ns/cm]. The second statistical test of the fit was a χ^2/degrees-of-freedom test [21,29,32] as a measure of goodness of fit: Here, χ^2 is 2.38, the sum of the squared residuals with four degrees of freedom (d.o.f.) (six residuals minus two fit parameters), and $\chi^2_4/4$ is 0.60. Statistical tables [33] give a 95% confidence interval for $\chi^2_4/4$ of 0.121–2.7856. Hence, at this confidence level, there is no evidence to suggest that the fit of these data to Eq. (4) is either too good to be true, unbelievable, or due to outliers in the data.

Regressions were applied to the arrival times for each method in Table II, and the corresponding fit parameters are shown in Table III. The top three lines pertain to raw data-arrival times on the system clock. Shown are (a) the intercept t_{bang} at $L = 0$ with its standard error and the corresponding 95% confidence interval and (b) the slope $(\bar{u})^{-1}$ (ns/cm) and its standard error (ns/cm). [To save space here, 3100 ns has been subtracted from t_{bang} and its confidence interval; that is, "8.1" stands for $t_{bang} = 3108.1$ ns, and "[6.1,10.1]" stands for a confidence interval of [3106.1, 3110.1 ns]. The intercept SE and the slope parameters may be read directly].

To visualize the results of Table III, Fig. 8 examines fits near $L = 0$. The upper part of this figure (in shades of blue and red) again refers to the fit of raw arrival times $\langle t\rangle^k_{FWHM}$ vs L_k in Fig. 7. According to Table III (top line), t_{bang} for this set of arrival times is 3108.06 ns; the red lines indicate a 95% confidence band of ±2 ns about t_{bang} (shown actual size). For L near 0 cm, one can just distinguish differences in the fit for the other raw estimates, t^k_{Mode} and t^k_{smoo} (lines 2 and 3, Table III): The light blue shaded band sketches the range of these fits and is truncated for $L > 2$ cm for clarity.

What effect on the t_{bang} parameter does correcting the raw arrival times for the individual, remaining parts

TABLE III. Fit statistics for shot 2584. For each method, the table lists the estimated intercept (bang time), its standard error SE (both in nanoseconds), and its estimated 95% CI, plus the slope and its standard error. For typographical convenience, 3100 ns has been arbitrarily subtracted from the fiducially referenced intercepts and CIs in this table. The $\langle t\rangle$corr entry includes the minor IRF corrections.

Method	Intrcpt:	SE (ns)	95% CI ns	Slope:	SE (ns/cm)
$\langle t\rangle$	8.1:	0.72	[6.1, 10.]	0.4631:	0.0006
t-mode	7.9:	0.69	[6.0, 9.9]	0.4623:	0.0005
t-smoo	8.2:	0.55	[6.6, 9.7]	0.4622:	0.0004
$\langle t\rangle$ corr	3.0:	0.97	[0.3, 5.6]	0.4646:	0.0007

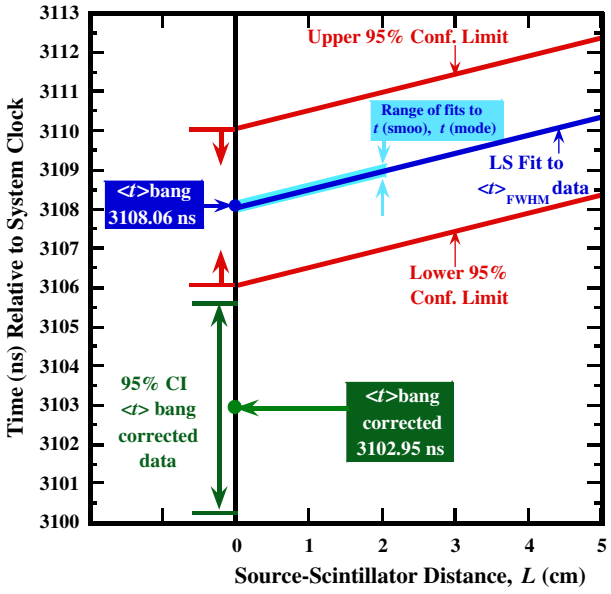

FIG. 8. Extrapolated region of arrival time-vs-distance fit curves for shot 2584. The dark blue fit line results from $\langle t\rangle_{\mathrm{FWHM}}$ data with 95% confidence uncertainty lines (red); extrapolated fits for the t_{Smoo} and t_{mode} data are indicated by the light blue line, truncated for clarity at 2 ns. The green lines below indicate the result for bang time and its uncertainty from $\langle t\rangle_{\mathrm{FWHM}}$ data after IRF corrections have been applied. The regression curve and its uncertainty band are not shown but are closely parallel to the raw data curves above.

(~3–5 ns, Fig. 2) of the IRF throughputs Δt_k have? Corrected parameters for the $\langle t\rangle^k_{\mathrm{FWHM}}$ data are shown on the bottom line, labeled $\langle t\rangle_{\mathrm{corr}}$ in Table III for comparison to the top line, labeled $\langle t\rangle$. Here, the raw mean arrival times were individually adjusted in time, and the resulting corrected times were regressed against distance. The net effect is to shift t_{bang} earlier by about 5 ns on the system clock with a slightly larger standard error and almost no change in slope. The lower part of Fig. 8 shows these differences graphically. Given the similarity in corrections to the arrival times, this shift is not surprising. On the basis of Table III and the previous statistical tests, one reports [34,35] a neutron $t_{\mathrm{bang}} = 3102.95$ ns with an SE $= 0.97$ ns and six measurements [or, equivalently, a CI of 3100.25–3105.60 ns]. The other arrival-time measures on correction gave similar results, but we have preferred the mean measure $\langle t\rangle^k_{\mathrm{FWHM}}$, which has a clearer mathematical claim on the convolution properties of Eq. (3) (Sec. III C) than do t_{smoo} and t_{mode}.

C. Estimating mean neutron speed $\bar{u}$ and $\bar{E}$

If one task of this nTOF diagnostic is an estimate of t_{bang}, the other is to see if neutrons from a $D(d,n)\mathrm{He}^3$ reaction are consistent with the slope $(\bar{u})^{-1}$ from Eq. (4), Table III. While this measurement does not detail the distribution of all the emitted neutrons in shot 2584, it can rule out thermalized or Maxwellian D-D distributions in the source plasma if the measured mean speed $\bar{u}$ differs appreciably from the expected value. One notes in Table III that the estimated slopes are nearly independent of both the arrival time method used and IRF corrections to the detector throughputs and have nearly identical standard errors. Using measure $\langle t\rangle_{\mathrm{corr}}$ in Table III, one has $\bar{u} = 2.1524 \pm 0.0032$ cm/ns (standard error) with six measurements [equivalently, a 95% CI of 2.144–2.1614 ns with four d.o.f.]. This estimate may be compared to the published value of 2.16018587 cm/ns, quoted by [12] for D-D fusion neutrons. Hence, here the results are consistent with the production of D-D fusion neutrons. An estimate of the average neutron energy $\bar{E}$ is then straightforward: The relativistic result $\bar{E} = m_0c^2[(1-\bar{u}^2/c^2)^{-1/2}-1]$ gives 2.4308 ± 0.022 MeV—or, alternatively, as a 2.409–2.453 MeV 95% CI with four d.o.f., which overlaps the published reference value of 2.4486857 MeV [12]. The corresponding classical result $\bar{E} = (1/2)m_0\bar{u}^2$ is 2.4216 ± 0.0144 MeV (standard error), or 2.4027–2.4419 MeV as a 95% CI, which does not quite overlap with the reference. (Here, m_0c^2 was taken as 939.565379 MeV and c as 29.9792458 cm/ns [12]).

V. DISCUSSION AND SUMMARY

To give further credence to the above results, one can estimate t_{bang} without a regression analysis if one is willing to assume the published value of $\bar{u}$ for the $D(d,n)^3\mathrm{He}$ reaction as a constant. That is, by summing the corrected arrival times [29,30] in Eq. (4), one obtains $\langle t_{\mathrm{bang}}\rangle_N \equiv N^{-1}\sum_{k=1}^{N}(\bar{t}_k - (\bar{u})^{-1}L_k) = 3105$ ns, which may be compared to $\langle t\rangle_{\mathrm{corr}} = 3103$ ns for the estimate from regression (Table III). Here, $N = 6$, $\bar{t}_k$ is the IRF-corrected mean travel times (at FWHM), and $\bar{u}$ is taken as 2.160 cm/ns [12]. See Table IV. One also notes the estimate $\langle t_{\mathrm{bang}}\rangle_N$ is the difference between two means (arrival times and times in flight) over N samples so that the effect of one odd, hypothetical error in arrival time [say, 2 ns for $\langle t\rangle_{5A1}$, noted in Sec. IV A] is partially averaged out by the rest of the sample times, in this case 2 ns/6 samples, or 333 ps on $\langle t_{\mathrm{bang}}\rangle_N$, which we have ignored.

TABLE IV. A comparison of parameter values and uncertainties by the regression analysis of Eq. (4) with corresponding values obtained under the *a priori* assumptions that uncertainties are $\delta L \sim 1$ cm and $\delta t \sim 1$ ns, respectively; the formulas are given in the text.

Parameter	By regression	By assumptions
t-bang (ns)	3103	3105
Unc. t-bang (ns)	0.97	0.50
u (cm/ns)	2.1524	2.1601*
Unc. u (cm/ns)	0.0032	0.0072

*This value is quoted by Ref. [12] and assumed in this estimate.

Although our reported uncertainty estimates for $t_{\rm bang}$ and $\bar{u}$ are based on the corrected data and the regression parameters (Table III), these uncertainties can also be estimated from the simple *a priori* uncertainty estimates ($\delta L \sim 1$ cm, $\delta t \sim 1$ ns) and error propagation. For example, under these conditions the uncertainty in $t_{\rm bang}$ can be estimated by summing Eq. (4) as above. Then, propagating both distance and time uncertainties, one estimates $(\delta t_{\rm bang})^2 \approx N^{-1}[(\delta t)^2 + (\delta L/\bar{u})^2]$, which by our assumptions gives $\delta t_{\rm bang} \approx 0.50$ ns and is comparable to the regression value (Table IV). In a similar way, it is possible to estimate the uncertainty $\delta\bar{u}$ in the speed estimate $\bar{u}$: e.g., $\bar{u} \approx L_k/(\bar{t}_k - t_{\rm bang})$, where $\bar{t}_k$ is again the IRF-corrected neutron arrival time at L_k. By error propagation, one now finds $(\delta\bar{u})^2(\bar{t}_k - t_{\rm bang})^2 \approx (\delta L_k)^2 + \bar{u}^2[(\delta t_k)^2 + (\delta t_{\rm bang})^2]$, where the statistical covariance between $\bar{t}_k$ and $t_{\rm bang}$ has been ignored. It is convenient to select the midpoint of the arrival time data in Fig. 6, taking $L = 945$ cm, $(\bar{t} - t_{\rm bang}) = 444$ ns, $\bar{u} = 2.16$ cm/ns, and $\delta t = \delta t_{\rm bang} \approx 1$ ns. The resulting uncertainty (Table IV) is $\delta\bar{u} \approx 0.0072$ cm/ns, which is comparable to the regression estimate in Table III. That these "back-of-the-envelope" estimates are comparable to the regression estimates suggests an internal consistency in the overall analysis of nTOF data and lends support to the basic assumptions made *a priori* to the analysis here.

Lastly, it was noted in Secs. II A and III A that, although the duration τ of the source is essentially ignorable for estimates of $t_{\rm bang}$ and $\bar{u}$, it can contribute to the FWHM $w^k_{\rm meas}$ of $D_k(t)$: $(w^k_{\rm meas})^2 \approx (w^k_{\rm spread})^2 + (3.5\ {\rm ns})^2 + \tau^2$ at each L_k, where $w^k_{\rm spread}$ is the Gaussian FWHM from Eq. (2) and 3.5 ns is the approximate FWHM of each nTOF detector. Briefly, if widths $w^k_{\rm meas}$ in Fig. 6 are corrected by 3.5 ns in quadrature and regressed upon L_k, then the intercept at $L = 0$ is an estimate of the source duration. The result is 3.25 ns (standard error, 0.84 ns, six measurements), or a 95% confidence interval of [0.91, 5.59] ns. [An uncertainty estimate of $(\delta\tau)$ can also be obtained by a simple, geometric argument and the estimate $\delta t \sim 1$ ns: Since the fit curve of N, FWHMs $w^k_{\rm spread}$ vs L_k passes through the point $(N^{-1}\Sigma_k L_k \approx 1144$ cm, $N^{-1}\Sigma_k w^k_{\rm spread})$, then by similar triangles one has $(\delta\tau) \approx (1\ {\rm ns})(1144\ {\rm cm})/(2510\text{–}1144\ {\rm cm}) = 0.84$ ns, as above].

In summary, this article describes a multichannel nTOF diagnostic suitable for neutron measurements at the Z accelerator and has been fielded on several developmental MagLIF shots. The analysis of nTOF data for shot 2584 is discussed here in detail, yielding estimates of the neutron bang time $t_{\rm bang}$ on the system clock and the mean speed $\bar{u}$ (with uncertainties) for neutrons generated in the shot. The method of analysis was based on (a) a plasma model due to Brysk [11], which assumes that the source plasma is uniform in temperature and particle density as well as Maxwellian; (b) signal traces in each channel were treated as Gaussian with linearly increasing arrival times and widths vs distance from the source; (c) definitions for times of arrival for the neutron pulses at a detector were defined and tested; (d) corrections were applied for the throughput response of the detectors; and (e) the arrival times were linearly regressed on distance from the neutron source to yield fit parameters related to $t_{\rm bang}$ and $\bar{u}$. Both the estimated $\bar{u}$ and mean kinetic energy $\bar{E}$ of the neutrons were consistent with the published values for DD fusion neutron reactions. With less precision, a source duration and its uncertainty was also obtained from pulse-width data.

ACKNOWLEDGMENTS

Sandia National Laboratories is a multimission laboratory managed and operated by National Technology and Engineering of Sandia, LLC, a wholly owned subsidiary of Honeywell International, Inc., for the U.S. Department of Energy's National Nuclear Security Administration under Contract No. DE-NA-0003525. The views expressed in the article do not necessarily represent the views of the U.S. Department of Energy or the United States Government. It is also a pleasure to thank our reviewers for their generous, patient, constructive criticism and suggestions for this article.

APPENDIX

For the nTOF experiments considered here, differing operational techniques were used to characterize a generic arrival time $\bar{t}_k$ for each data trace $D_k(t)$. Three procedures were chosen, yielding peak-time estimates that we label (a) $t_{\rm smoo}$, (b) $t_{\rm mode}$, and (c) $\langle t\rangle$. The first two refer to the statistical mode of the recorded traces: Specifically, $t_{\rm smoo}$ refers to a smoothed trace and $t_{\rm mode}$ to a raw trace (with noise); and the third measure $\langle t\rangle$ is a mean statistical value over a specified time interval. These measures are compared here for consistency using the noisiest raw data channel in shot 2584: BB1.

The Savitzke-Golay (SG) method was chosen for the $t_{\rm smoo}$ estimate. It is a low-pass digital filter for equally spaced time-domain data [21,22] and transforms a discrete, noisy signal, like $D_k(t)$, into a smoothed signal $D^{\rm smoo}_k(t)$, based on local polynomial fits. (Both the polynomial degree and the width of the averaging window can be selected).

Figure 9 shows the results of applying this method to $D_{\rm BB1}(t)$ in Fig. 3. The filter comprised a fourth-degree polynomial with a 21-point smoothing window over the 201 points between 3400 ns $\le t \le$ 3450 ns. Both the raw data and smoothed result $D^{\rm smoo}_{\rm BB1}(t)$ are shown for comparison. The visual agreement between $D_{\rm BB1}(t)$ and $D^{\rm smoo}_{\rm BB1}(t)$ is qualitatively very close in each of these regions, with scant evidence on this scale of systematic distortion in $D^{\rm smoo}_{\rm BB1}(t)$. But the real utility of this method is that both $D^{\rm smoo}_{\rm BB1}(t)$ and

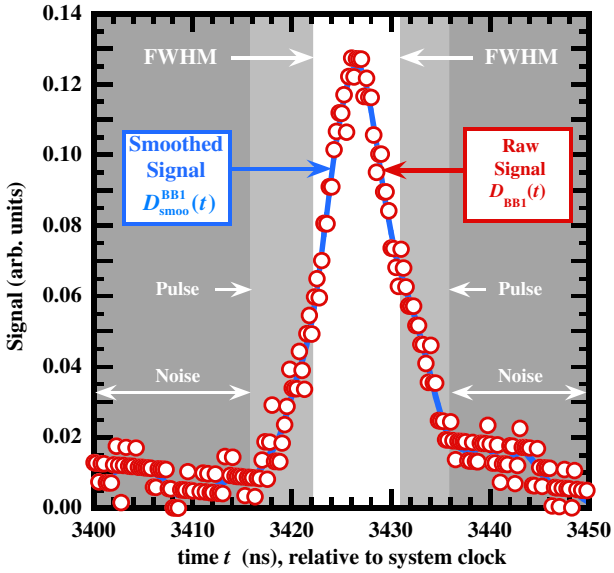

FIG. 9. Comparison of the data pulse for channel bb1 vs the signal smoothed by the Savitzky-Golay digital filter. The peak parameter t_{smoo} is thus calculated from the entire raw signal. Arbitrarily defined subdomains (noise, pulse, and FWHM) are indicated.

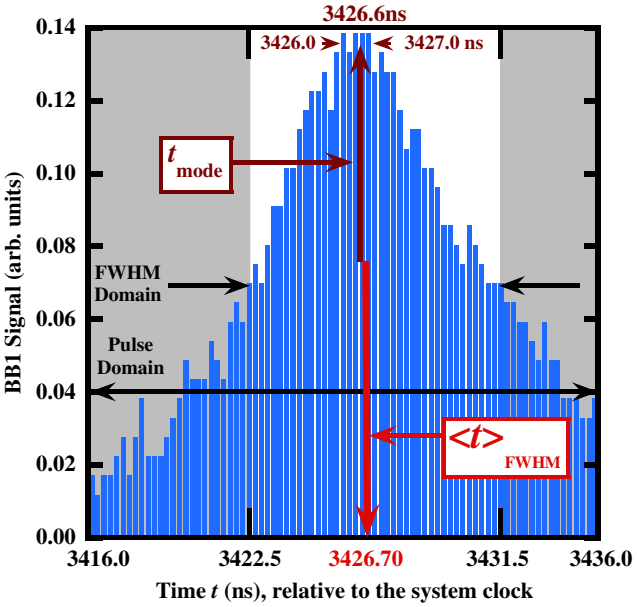

FIG. 11. BB1 portrayed as a pulse-height distribution in the FWHM and pulse domains with corresponding peak measures t_{mode} and $\langle t\rangle_{FWHM}$.

its derivative are smooth, so that the smoothed-signal mode t^{BB1}_{smoo} can be precisely defined where $\partial D^{BB1}_{smoo}/\partial t$ crosses 0. This estimate is shown in shown in Fig. 10, where $t_{smoo} =$ 3426.50 ns with a resolution uncertainty of less than 1 ns.

The second estimate of time at peak t^{BB1}_{mode} is defined simply by the largest value of the raw data $D_{BB1}(t)$. This is a crude "eyeball" method, requiring some arbitrary averaging if there is no unique maximum signal value near the peak. The value 3426.6 ns (dark red arrow) is shown at the top in Fig. 11, where $D_{BB1}(t)$ is shown as a binned pulse-height distribution. (Four nearby values were averaged for this estimate.)

The third estimate of arrival time was the statistical mean $\langle t\rangle \equiv [\Sigma^N_{j=1} t_j D(t_j)]/[(\Sigma^N_{j=1} D(t_j)]$ over a specified time interval or bins. This result is also shown at the bottom in Fig. 11 (bright red arrow). Because of signal noise, background signals, and the IRF, $\langle t\rangle^{BB1}$ does depend on the time interval. Figure 11 highlights two such windows: the FWHM of the pulse region and a larger region containing more of the skewed fall time of the pulse (labeled pulse domain). One finds that $\langle t\rangle^{BB1}_{FWHM} = 3426.7$ ns (33 pts) for the FWHM region and $\langle t\rangle^{BB1}_{PULSE} = 3426.8$ ns (80 pts) for the wider domain ns.

In summary, one has three recorded "arrival-time" measures for the BB1 signal in shot 2584 ranging from 3426.5 to 3426.7 ns.

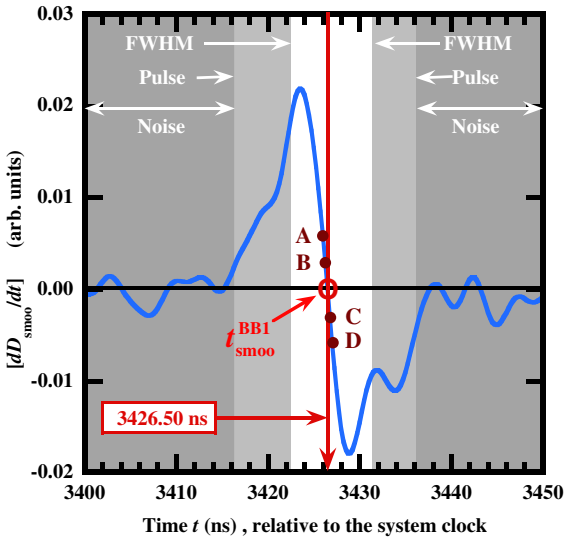

FIG. 10. The first derivative of D_{smoo} vs time. The peak time t_{smoo}, taken where $dD_{smoo}/dt = 0$, is indicated. For reference, derivative values for adjacent time values are shown: (a) 3426.00 ns, (b) 3426.25 ns, (c) 3426.75 ns, and (d) 3427.00.

[1] R. B. Spielman *et al.*, Tungsten wire-array Z-pinch experiments at 200 TW and 2 MJ, Phys. Plasmas **5**, 2105 (1998).
[2] W. A. Stygar *et al.*, X-ray emission from z pinches at 10^7 A: Current scaling, gap closure, and shot-to-shot fluctuations, Phys. Rev. E **69**, 046403 (2004).
[3] S. A. Slutz, M. C. Herrmann, R. A. Vesey, A. B. Sefkow, D. B. Sinars, D. C. Rovang, K. J. Peterson, and M. E. Cuneo, Pulsed-power-driven cylindrical liner implosions of laser preheated fuel magnetized with an axial field, Phys. Plasmas **17**, 056303 (2010).

[4] M. R. Gomez, *et al.*, Experimental Demonstration of Fusion-Relevant Conditions in Magnetized Liner Inertial Fusion, Phys. Rev. Lett. **113**, 155003 (2014).

[5] K. D. Hahn *et al.*, Fusion-neutron measurements for magnetized liner inertial fusion experiments on the Z accelerator, J. Phys. Conf. Ser. **717**, 012020 (2016).

[6] K. D. Hahn, C. L. Ruiz, G. W. Cooper, A. J. Nelson, G. A. Chandler, R. J. Leeper, B. R. McWatters, R. Smelser, and J. A. Torres, Calibration of neutron-yield diagnostics in attenuating and scattering environments, Rev. Sci. Instrum. **83**, 10D914 (2012).

[7] S. Hanson, Progress in Magnetized Liner Inertial Fusion (MagLIF), in *Proceedings of the 42nd European Physical Society Conference on Plasma Physics, Lisbon, Portugal* (2015).

[8] I. F. Zartman, A direct measurement of molecular velocities, Phys. Rev. **37**, 383 (1931).

[9] C. Ko, The heat of dissociation of Bi_2 determined by the method of molecular beams, J. Franklin Inst. **217**, 173 (1934).

[10] L. C. L. Yuan and S. J. Lindenbaum, Determination of Velocity: Time-of-Flight Method, Sect. 2.2.1.3.1, *Methods of Experimental Physics A*, edited by L. C. L. Yuan and C.-S. Wu, Nuclear Physics, part A (Academic, New York, 1961), 438 ff.

[11] H. Brysk, Fusion neutron energies and spectra, Plasma Phys. **15**, 611 (1973).

[12] D. H. Munro, Interpreting inertial fusion neutron spectra, Nucl. Fusion **56**, 036001 (2016).

[13] L. Ballabio, J. Kallne, and G. Gorini, Relativistic calculation of fusion product spectra for thermonuclear plasmas, Nucl. Fusion **38**, 1723 (1998).

[14] V. Y. Glebov *et al.*, The National Ignition Facility neutron time-of-flight system and its initial performance (invited), Rev. Sci. Instrum. **81**, 10D325 (2010).

[15] R. Hatarik, D. B. Sayre, J. A. Caggiano, T. Phillips, M. J. Eckart, E. J. Bond, C. Cerjan, G. P. Grim, E. P. Hartouni, J. P. Knauer, J. M. Mcnaney, and D. H. Munro, Analysis of the neutron time-of-flight spectra from inertial confinement fusion experiments, J. Appl. Phys. **118**, 184502 (2015).

[16] 16. T. J. Murphy, R. E. Chrien, and K. A. Klare, Interpretation of neutron time-of-flight signals from current-mode detectors, Rev. Sci. Instrum. **68**, 610 (1997).

[17] T. J. Murphy, R. A. Lerche, C. Bennett, and G. Howe, Ion-temperature measurement of indirectly driven implosions using a geometry-compensated neutron time-of-flight detector, Rev. Sci. Instrum. **66**, 930 (1995).

[18] T. J. Murphy, J. L Jimerson, R. R. Bergren, J. R. Faulkner, J. A Oertel, and P. J. Walsh, Neutron time-of-flight and emission time diagnostics for the National Ignition Facility, Rev. Sci. Instrum. **72**, 850 (2001).

[19] C. L. Ruiz, G. W. Cooper, S. A. Slutz, J. E. Bailey, G. A. Chandler, T. J. Nash, T. A. Mehlhorn, R. J. Leeper, D. L. Fehl, A. J. Nelson, J. Franklin, and L. Ziegler, Production of Thermonuclear Neutrons from Deuterium-Filled Capsule Implosions Driven by *Z*-Pinch Dynamic Hohlraums, Phys. Rev. Lett. **93**, 015001 (2004).

[20] M. A Bonura, C. L. Ruiz, D. L. Fehl, G. W. Cooper, G. Chandler, K. D. Hahn, A. J. Nelson, J. D. Styron, and J. A. Torres, A technique for verifying the input response function of neutron time-of-flight scintillation detectors using cosmic rays, Rev. Sci. Instrum. **85**, 11D633 (2014).

[21] W. H. Press, S. A. Teukolsky, W. T. Vetterling, and B. P. Flannery, *Numerical Recipes in FORTRAN: The Art of Scientific Computing*, 2nd ed. (Cambridge University Press, Cambridge, England, 1992), Sec. 14.8, 644 ff.

[22] Wikipedia, Savitzky-Golay filter, https://en.wikipedia.org/wiki/Savitzky_Golay_filter.

[23] H. H. Barrett and W. Swindell, *Radiological Imaging: The Theory of Image Formation, Detection, and Processing* (Academic Press, New York, 1981), Vol. 1.

[24] M. Bertero, Linear Inverse and Ill-Posed Problems, in *Advances in Electronics and Electron Physics*, Vol. 75, edited by P. W. Hawkes (Academic, Harcourt Brace Jovanovich, Boston, 1989), pp. 2–120.

[25] I. J. D. Craig and J. C. Brown, *Inverse Problems in Astronomy: A Guide to Inversion Strategies for Remotely Sensed Data* (Adam Hilger, Boston, 1986), Sec. IV. 3.

[26] G. M. Wing, *A Primer on Integral Equations of the First Kind: The Problem of Deconvolution and Unfolding* (Society for Industrial and Applied Mathematics, SIAM, Philadelphia, 1991), p. 71.

[27] D. L. Fehl, G. A. Chandler, W. A. Stygar, R. E. Olson, C. L. Ruiz, J. J. Hohlfelder, L. P. Mix, F. Biggs, M. Berninger, P. O. Frederickson, and R. Frederickson, Characterization and error analysis of an $N \times N$ unfolding procedure applied to filtered, photoelectric x-ray detector arrays. I. Formulation and testing, Phys. Rev. Accel. Beams **13**, 120402 (2010).

[28] R. N. Bracewell, *The Fourier Transform and Its Applications*, 2nd ed. (McGraw-Hill, New York, 1978), pp. 108–119.

[29] J. Neter, M. H. Kutner, C. J. Nachtsheim, and W. Wasserman, *Applied Linear Regression Models*, 3rd ed. (R. D. Erwin, Inc., Chicago, 1996).

[30] K. A. Brownlee, *Statistical Theory and Methodology in Science and Engineering*, 2nd ed. (Wiley, New York, 1965).

[31] S. L. Meyer, *Data Analysis for Scientists and Engineers* Wiley, New York, 1975).

[32] M. G. Natrella, *Experimental Statistics* (Dover, Mineola, NY, 2005, a republication of National Bureau of Standards Handbook 91, issued in 1963), Chap. 5.

[33] *CRC Standard Probability and Statistics Tables and Formulae*, edited by W. H. Beyer (CRC, Boca Raton, FL, 1991), pp. 207–209.

[34] B. N. Taylor and C. E. Kuyatt, Guidelines for Evaluating and Expressing the Uncertainty of NIST Measurement Results, *NIST Technical Note 1297* (National Institute of Standards and Technology, Gaithersburg, 1994).

[35] T. M. Adams, G104—A2LA Guide for Estimation of Measurement Uncertainty in Testing, 2014, https://portal.A2LA.org/guidance/est_mu_testing.pdf.